

Figure 2: Schematic view of the injection straight in the horizontal (upper) and vertical (lower) plane.

Stripping foil

The H⁻ charge stripping foil is very difficult part of the RCS. The energy deposition onto foil by the incoming H⁻ and the circulating proton beams amounts to 5.8 watts per beam area in average, and 460 watts at peak. The temperature rise was calculated by ANSYS, taking into account the distributions of energy deposition onto foil. Although the temperature depends upon the emissivity (ϵ) of the hot foil surface, it reached ~1500K at peak with $\epsilon=0.2$. Such high energy deposition may cause a shorter lifetime of the foil, i.e. the foil breaks up or deforms seriously in a short time. Development of foils against such deteriorations is urgent [5, 6]. Fig.3 shows the deformation of the H⁻ stripping foil which was used at the KEK PS booster synchrotron: the injection energy is 40MeV, and the average energy deposition is 0.73 watts.

Bump magnets

The bump system requires fast and flexible current pattern power supplies. Fig.4 shows the current waveforms of each magnet. The horizontal paint waveform follows $1 - \sqrt{t/T}$, the vertical anti-correlated one $\sqrt{1-t/T}$, and the vertical correlated one $\sqrt{t/T}$, where T is the injection period, ~500 μ sec. Specifications for such bump power supply are listed in Table 2. These comprise rectifier and chopper sections, which utilize many high power IGBT's (Insulated Gate Bipolar Transistor) in series and/or parallel to realize the high power operation with a tracking error less than 1%.

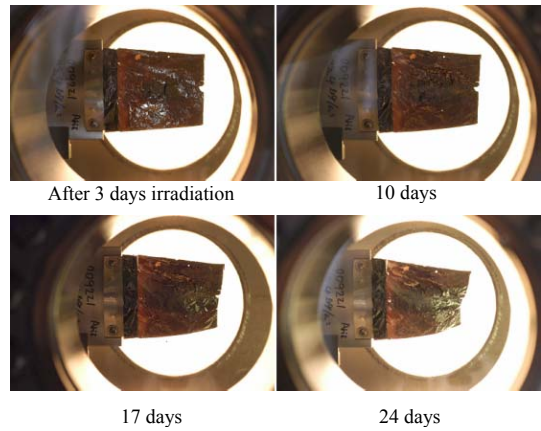


Figure 3: Deformations of H⁻ stripping foil at the KEK PS booster synchrotron (courtesy of Y. Arakida)

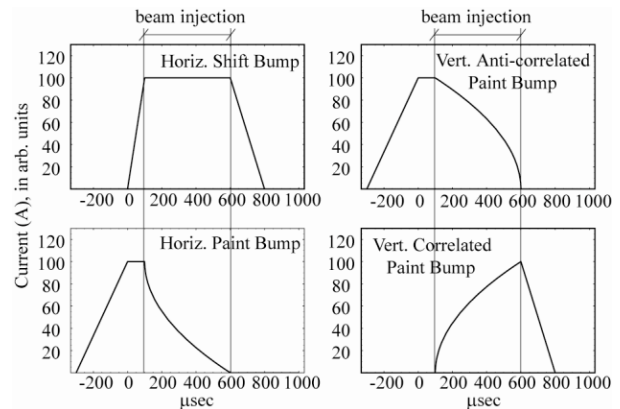


Figure 4: Current waveforms of painting injection

Table 2: Specifications for the bump power supply. Tracking error is 1%.

Power supply	No.	Voltage (KV)	Current (KA)	IGBT rating	effective carrier frequency (KHz)
Horiz. SB	1	10.0	32.2	3300V, 1200A	60
Horiz. PB	4	1.2	29.0	1200V, 300A	1800
Vert. PB	2	0.6	3.4	1200V, 300A	1800

RF

Higher RF voltage gain is a remarkable aspect of the RCS, where the peak RF voltage per turn is 450KV. A high gradient cavity has been developed at KEK for this purpose [7], which is capable of producing more than twice as much as the voltage of the conventional ferrite loaded cavity. The high gradient cavity is made of the magnetic alloy (MA), and is of a broadband resonator, the resonant frequency of which is located near at the middle point of the acceleration frequency range. The cavity impedance then shows capacitive at an early acceleration stage, and inductive at a later stage for the fundamental RF frequency: actually, phase angle of the

cavity is 42 degrees at injection, and -24 degrees at extraction with the resonant frequency at 1.5MHz, and the unloaded cavity $Q=2.0$. the unloaded Q value can be adjusted by cutting the core and binding together with a small gap between two halves (Fig.5). High power test of the MA cavity was carried out successfully for eight hours with 14KV/gap, 30% duty factor at 1.3MHz [8]. RF parameters are summarized in Table 3.

Second harmonic component is superimposed on the same cavity to improve the bunching factor [9].

$$V_{rf} = V_1 \sin \phi + V_2 \sin 2(\phi - \phi_s + \phi_2),$$

$$V_2 = 0.8 V_1 \cos \phi_s,$$

where V_1 is the fundamental RF voltage, V_2 the second harmonic voltage, V_{rf} the total voltage, and ϕ_s the synchronous phase angle. The optimization of the offset (ϕ_2) has been investigated during the injection period. The offset was so varied that it starts with an initial value (ϕ_2^0) and then decreases linearly with time down to zero at the injection end. Fig.6 shows the results for $\phi_2^0=20, 25$ and 30 degrees. It is found that the phase error of only 5 degrees will cause the difference of the bunching factor by ~ 0.05 . In the figure are also shown the harmonic contents in the trapping and early stage of acceleration. Fundamental component reaches 10A after the injection end, and the higher harmonics amount to a few tenths of the fundamental one. Relative loading Y (=beam current/generator current) then becomes 1.2, the beam loading cancellations of these components are essential for the precise control of the system. In the J-PARC, a feedforward cancellation will be employed by means of the digital techniques [10].



Figure 5: MA cut core (left) and the MA loaded cavity (right).

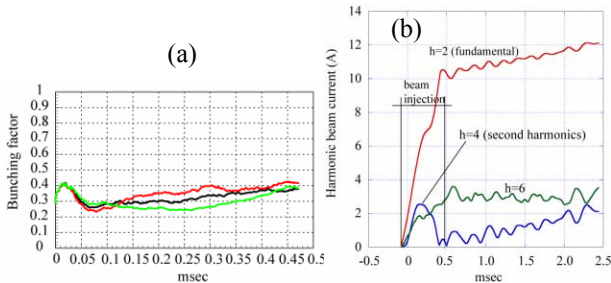


Figure 6: (a)Variation of bunching factor. Initial phase of the second harmonic cavity to the fundamental one is 25deg. (black), 30deg. (red) and 20deg. (green). (b)Harmonic contents in the trapping and early stage of acceleration

Table 3: RF parameters.

Number of cavities		11
Length of cavity	m	2
Voltage per cavity	KV	45
Number of gaps per cavity		3
Number of MA cores per cavity		18
Unloaded Q value		~ 2
Impedance per gap	Ω	~ 840
Impedance per cavity (seen by the beam)	Ω	$\sim 1,800$
Resonant frequency	MHz	~ 1.5
Operating frequency	MHz	0.9~5.1
Beam loading		
beam current	A	8.2~11.1
fundamental component	A	10~21
second harmonic	A	< 18
third harmonic	A	< 13
RF amplifier		TH558 $\times 2$ in push-pull mode
Anode power supply		
output voltage	KV	10
output current	A	120

MAGNETS

In order to cover a wider range of the RCS operation tunes, the quadrupole magnets have been grouped into seven families with different dimensions [11]. All the magnets within a family are connected in series to the power supply, and are fed by the dc-biased sinusoidal ac current. As for the bending magnets, since the excitation current is much higher than those of the quadrupole magnets, the power supply is divided into the ac and dc supplies, which comprise the White circuit [12].

Field saturation of the dipole magnet has been observed by the field calculations using TOSCA and POISSON (Fig.7). In the figure, degradation of the magnet inductance implies the field saturation. Since the quadrupole magnet is not saturated within a range of use, field gradient is assumed to vary in a ideal sinusoidal waveform. The tracking error of the quadrupole magnets to the dipole magnet field can then be calculated in the following [13]:

$$\frac{\Delta K}{K} = \frac{1 - \alpha \cos \omega t}{1 + \frac{a_2}{B_{dc}} - \alpha \cos \omega t \left(1 - 3 \frac{a_3}{a_1} + 2 \frac{a_2}{a_1} \cos \omega t + 4 \frac{a_3}{a_1} \cos^2 \omega t\right)} - 1,$$

where $\alpha=B_{ac}/B_{dc}=0.6$ and the saturated ac field is expressed as,

$$B_{ac}(t) = a_1 \cos \omega t + a_2 \cos 2\omega t + a_3 \cos 3\omega t.$$

From the saturated field data, each coefficient is given by $a_1=0.44411$, $a_2=0.0024$ and $a_3=0.001392$. Fig.8 shows the tracking error, reaching its maximum of 1.3% at injection without any harmonic corrections. The tune shift caused by this error is estimated to be 0.12. Therefore, the correction of the field distortions is essential.

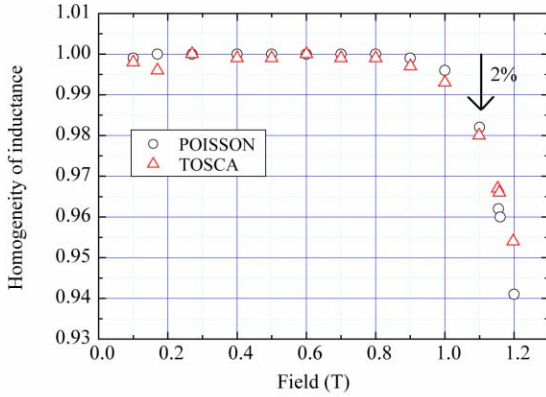


Figure 7: Field saturation of the dipole magnet. Horizontal axis shows the ideal field produced by a given coil current [12].

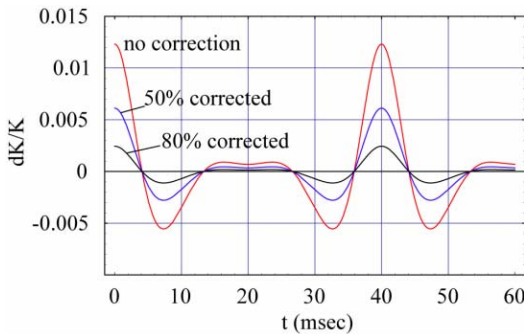


Figure 8: Tracking error due to the field saturation of the dipole magnet. The magnet field is swept at 25Hz repetition.

CERAMIC CHAMBER

The ceramic vacuum chambers are used at the ac and pulsed magnet sections in order to avoid an excessive heating by the alternating magnetic field. However, copper stripes of RF shield are electrotyped on the outer surface of the chamber in order to provide a path for an image current of the circulating beam as in Fig.9 [14]. Typical cross section of the copper stripe is 5mm-wide and 0.5mm-thick, and is arranged in 10mm pitch. The one end of the RF shield is directly connected to the Ti flange, and the other end is terminated by the $\sim 0.1\mu\text{F}$ capacitor to the flange. The eddy field and the heating of the stripes are negligible. The inner surface of the ceramic chamber is coated by TiN to suppress the secondary electron emission.

Roundness and straightness measurements have been performed for circular chambers. The results show that, for chambers without any polishing or grinding after sintering, the roundness is several hundred micron and the straightness less than 1mm [15]. However, regarding the ceramic chambers which have very asymmetrical shape as in Fig.10, may require R&D to assure the uniformity after sintering.

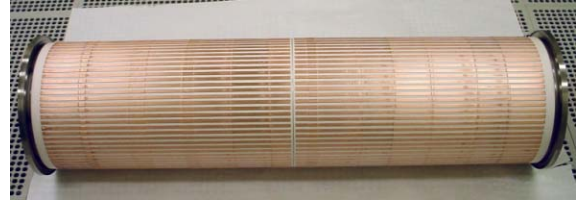


Figure 9: Circular ceramic chamber, 260 mm-diameter, 1,200 mm-long with 100 lines of rf shield on the outer surface. Two segments are joined by brazing at the center.

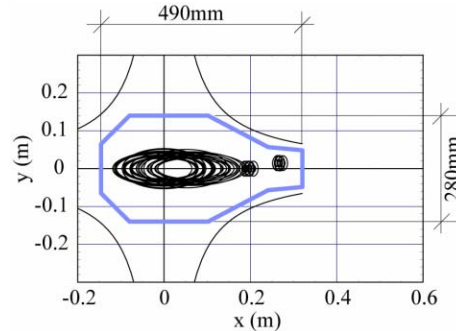


Figure 10: Ceramic chamber at the injection quadrupole with a pear-like cross section. The central large ellipses shows the circulating beam, and the small ellipses at the right hand side the incoming H beam.

ELECTRON-PROTON INSTABILITY

The electron-proton instability is thought to be strong and fast instability for the high intensity machine [16]. Electrons in the proton ring can be produced by proton loss, electron stripping at the charge exchange foil and ionization of the residual gas. The electron cloud is formed by the trailing-edge multipacting process, and strongly depends upon the parameters such as primary electron production rate (Y_1), secondary electron yield (Y_2), beam size, chamber size, bunch length and bunch spacing. Ohmi *et al* [17] assumed $Y_1=4.4 \times 10^{-6} \text{e}/(\text{meter} \cdot \text{proton})$ and

$$Y_2(E) = Y_{2,\text{max}} \frac{E}{E_{\text{max}}} \frac{1.44}{0.44 + (E/E_{\text{max}})^{1.44}},$$

where $Y_{2,\text{max}}=2.1$, E the energy of primary electrons and $E_{\text{max}}=200\text{eV}$ by the measurements for the aluminum surface[18]. The electron amplification factor (A_e) is defined by the number of the created electrons normalized to that of the primary electrons as a function of a distance traversed (s), ie $A_e(s)=\lambda_e(s)/(Y_1 N_p)$. Fig.11 shows the amplification factors. The stability criterion is described in terms of the neutralization, which is given by the ratio of the electron cloud line density to the average proton density. Assuming the proton bunch length is very long compared with the dipole mode frequency of the electrons, the coasting beam approximation is used. Table 4 shows the neutralizations at the peak and bottom of the amplification curve, and the threshold neutralization [17]. Hence, injection stage

of the 3GeV RCS and the ISIS synchrotron is safe for the electron-proton instability, but it is likely to occur at the Los Alamos Laboratory's Proton Storage Ring (PSR) and the Oak Ridge Laboratory's Spallation Neutron Source (SNS) storage rings.

These results are, however, drastically changed if different assumptions are adopted. Taking $Y_{2,max}=1.5$ which is the case for TiN coated surface, the neutralizations at the peak and bottom become 0.006 and 0.0038, respectively at the PSR [19], which are now well below the threshold value of 0.021. Also, it should be required to identify the proton loss rate in the actual machines: for example, primary electrons coming from the stripping process at the foil is neglected in the present calculations. It is prudent, however, to have provisions of TiN coating and a weak solenoid in the ring to suppress the multipacting [20]

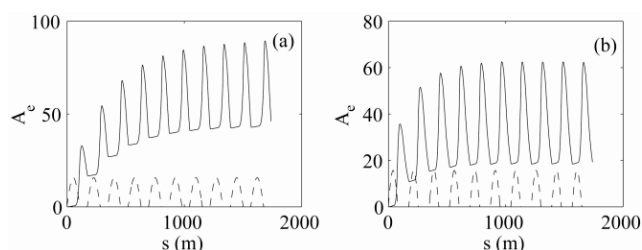


Figure 11: Electron amplification factors by the simulation for (a) 3 GeV RCS injection and (b) extraction. The proton beam bunch shapes are plotted by the dashed lines with arbitrary units [17].

Table 4: Neutralization factor (f). The bottom and peak values are taken at the stationary state in the calculations of the electron amplification factor.

neutralization	3GeV RCS		PSR	ISIS	SNS
	injection	extraction			
f(bottom)	0.020	0.007	0.034	0.003	0.007
f(peak)	0.042	0.023	0.067	0.005	0.250
f(threshold)	0.280	0.030	0.021	0.417	0.063

REFERENCES

[1] The NSNS Collaboration, Vol.1, NSNS/CDR-2/V1, May 1997.
 [2] JAERI/KEK Joint Project Team, KEK Report 2002-13, JAERI-Tech 2003-044, March 2003.
 [3] I.Sakai *et al*, 2003 PAC, Portland, p.1512.
 [4] M.Shirakata, H.Fujimori, Y.Irie, this conference.
 [5] I.Sugai *et al*, Nucl. Instrum. Methods Phys. Res. A 521, 2004, p.192.
 [6] R.W.Shaw *et al*, 2003 PAC, Portland, p.617.
 [7] C.Ohmori *et al*, PAC 97, Vancouver, p.2995.
 [8] M.Yoshii, private communications.
 [9] M.Yamamoto *et al*, EPAC 2002, Paris, p.1073.
 [10] F.Tamura *et al*, EPAC 2002, Paris, p.2106.
 [11] N.Tani *et al*, 18th Int. Conf. Magnet Technology, October, 2003, Morioka, 2B-a04.
 [12] M.G.White, F.C.Shoemaker and G.K.O'Neill, CERN Symposium, 1956, p.525.

RADIATION PROTECTION

Given proton losses in KW, the residual radioactivity and absorbed dose at the beam collimator region were compared for the variety of injection energies by means of the MARS code [21]. The total loss of protons in the ring was assumed to be 3.6KW for all cases, and the collimator section in the old JHF 3GeV ring was used for the model calculations [22]. Fig.12 shows the results for a quadrupole magnet next to the primary collimator. It is seen that the residual and absorbed dose rates increase with the injection energy.

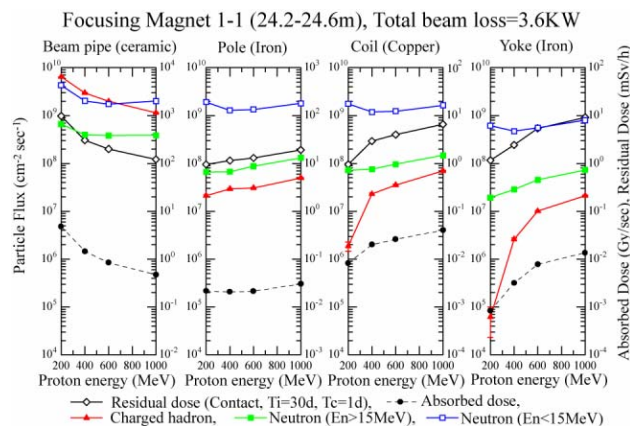


Figure 12: Energy dependence of particle flux, residual and absorbed dose rate for a quadrupole magnet at the collimator section.

[13] T.Adachi, Internal memo, KEK, 2001 (in Japanese).
 [14] M.Kinsho *et al*, Vacuum 73 (2004), p.187.
 [15] D.Nishizawa *et al*, JAERI-Tech 2001-081 (In Japanese).
 [16] R.J.Macek *et al*, 2001 PAC, Chicago, p.688.
 [17] K.Ohmi, T.Toyama and C.Ohmori, Phys. Rev. ST-Accelerators and Beams, Vol.5, 114402 (2002). Erratum, Vol.6, 029901 (2003)
 [18] T.Toyama, Y.Irie, S.Kato, K.Ohmi, C.Ohmori, K.Satoh and M.Uota, CERN Yellow Report 2002-001, 2002.
 [19] K.Ohmi, private communications.
 [20] L.F.Wang, D.Raparia, J.Wei and S.Y.Zhang, Phys. Rev. ST- Accelerators and Beams, Vol.7, 034401 (2004).
 [21] N. Mokhov, FERMILAB-FN-628, 1995.
 [22] N.Nakao *et al*, EPAC 2000, Vienna, p.2402.